applied sciences

MDPI

Article

Characterisation of Coastal Sediment Properties from Spectral Reflectance Data

Jasper Knight [1,*] and Mohamed A. M. Abd Elbasit [2]

[1] School of Geography, Archaeology & Environmental Studies, University of the Witwatersrand, Johannesburg 2050, South Africa
[2] School of Natural and Applied Sciences, Sol Plaatje University, Kimberley 8301, South Africa; mohamed.ahmed@spu.ac.za
* Correspondence: jasper.knight@wits.ac.za

Abstract: Remote sensing of coastal sediments for the purpose of automated mapping of their physical properties (grain size, mineralogy and carbonate content) across space has not been widely applied globally or in South Africa. This paper describes a baseline study towards achieving this aim by examining the spectral reflectance signatures of field sediment samples from a beach–dune system at Oyster Bay, Eastern Cape, South Africa. Laboratory measurements of grain size and carbonate content of field samples (n = 134) were compared to laboratory measurements of the spectral signature of these samples using an analytical spectral device (ASD), and the results interrogated using different statistical methods. These results show that the proportion of fine sand, $CaCO_3$ content and the distributional range of sediment grain sizes within a sample (here termed *span*) are the parameters with greatest statistical significance—and thus greatest potential interpretive value—with respect to their spectral signatures measured by the ASD. These parameters are also statistically associated with specific wavebands in the visible and near infrared, and the shortwave infrared parts of the spectrum. These results show the potential of spectral reflectance data for discriminating elements of grain size properties of coastal sediments, and thus can provide the baseline towards achieving automated spatial mapping of sediment properties across coastal beach–dune environments using hyperspectral remote sensing techniques.

Keywords: grain size analysis; coastal sediments; analytical spectral device; hyperspectral data

Citation: Knight, J.; Abd Elbasit, M.A.M. Characterisation of Coastal Sediment Properties from Spectral Reflectance Data. *Appl. Sci.* **2022**, *12*, 6826. https://doi.org/10.3390/app12136826

Academic Editors: Giovanni Randazzo, Stefania Lanza and Anselme Muzirafuti

Received: 9 May 2022
Accepted: 3 June 2022
Published: 5 July 2022

1. Introduction

Sediment properties of sandy beaches and sand dunes, including grain size, carbonate content, moisture content, organic content, magnetic susceptibility and grain mineralogy, are most commonly measured and quantified based on field observations or field sampling, and then laboratory analysis of these samples using different analytical equipment [1–4]. Following this, a range of statistical techniques (e.g., calculation of moment measures, multivariate analyses) can be used on the grain size data in particular, in order to characterise sediment properties and to interpret depositional processes and environments and their changes over time and space, e.g., [5–11]. This standard methodology has been undertaken on many beaches and dunes worldwide, resulting in an understanding of spatial patterns of different sediment properties (based mainly on grain size) across different coastal depositional environments, e.g., [12–15]. The main problem of such a field-based approach is that it provides only a limited view of local-scale coastal sediment properties and dynamics, which is often strongly affected by the specific spatial and temporal context of field sampling at individual sites. In addition, studies also use different sampling strategies and methods of data analysis, which means that results from these individual studies may not be comparable. By contrast, remote sensing methods using a variety of platforms have potential to consistently map and quantify spatial patterns of sediments and landforms across beach–dune systems, and this has been undertaken in several studies e.g., [16–21]. There

are fewer studies, however, that have examined spectral data on sediment properties and stratigraphy. Sediment cores have been examined using different hyperspectral imaging techniques, mainly in the shortwave infrared (SWIR) wavebands, in order to identify stratigraphic variations in sediment grain size and mineralogy [22–24]. These studies have been used to produce spectral time series maps that represent variations in sediment properties through the cores, rather than identify individual spectra that represent certain sediment endmembers. There are only a few studies that have examined the spectral properties of sediments in coastal environments, and these have considered the role of variations in water content and mineralogy as key factors influencing their spectral signatures [18,25]. Mineral compositions can then be used to derive endmembers for spatial modelling.

Most work on spectral signatures of sediment has been done on river depositional environments [26,27], and work on coastal sediments can be informed by these previous studies. For example, river and coastal sediment samples in NE Italy were evaluated by Ciampalini et al. [28] using an analytical spectral device (ASD) in order to derive a spectral library representing sample grain size and mineralogy, which was then compared to laboratory results. Principal component analysis was then used to identify sediment provenance endmembers. The same research approach was used by Ibrahim et al. [19] along the Belgian coast. Grain size properties along beaches were examined using Landsat visible, near infrared (VNIR) and thermal infrared bands in SE India [29], but these bands may have been influenced by a high concentration of heavy minerals (50–80%) at this site. Using IKONOS imagery, Park et al. [30] showed that all spectral bands have a good correlation (>0.8) with grain size, and Williams and Greeley [31] showed that different spectral bands from synthetic aperture radar imagery are affected by surface moisture. Thus, there are several studies that have analysed the spectral properties of beach sand but these have tended to focus on the role of local environmental factors rather than the application of different techniques or methodologies. A key question is how location-specific measurements can be applied to similar depositional settings elsewhere [27,32] or how patterns of (for example) grain size, calcium carbonate ($CaCO_3$), organic carbon or biomass content can be mapped across space using automated remote sensing techniques [21,33–35].

Although field and laboratory hyperspectral devices have been used to derive data on coastal sediment properties [16,28,36], there have been hitherto no published studies using the spectral properties of sediments from coastal settings in South Africa. This study uses laboratory hyperspectral measurements of sediment samples collected from a beach–dune system on the coast of South Africa, focusing on relationships between selected properties of the field samples (including grain size and carbonate content) and their associated spectral signatures. The aims of this study are to describe the nature of beach–dune samples in terms of their spectral signatures and to examine these relationships using statistical methods. This can be considered as a first step towards developing a robust methodology for automated mapping of sediment properties across beach–dune environments applicable globally.

2. Study Area and Methods

The study area examined, from which surface sediments were sampled, is at Oyster Bay, Eastern Cape Province, South Africa (Figure 1). Prevailing winds in this region are towards the northeast (in summer) and the west/northwest (in winter). Tidal range is high microtidal/low mesotidal and swell waves from the Southern Ocean have a significant wave height of >5 m [37]. Oyster Bay is an asymmetrical zeta-shape embayment [38] with an extensive sandy beach that is 6.1 km in total length and with a variable beach width of 30 to 290 m at low tide. Bedrock headlands to the east and west define the overall shape of the bay. An extensive supratidal zone is present, containing parallel-aligned transverse dunes with crests that are 40–50 m apart, similar to those found elsewhere along the South African coast [39]. Dune migration periodically blocks off the mouth of the incoming Klipdrift River. The landward boundary of the supratidal dunes at the back of the beach is marked by dune migration into a zone of highly vegetated and variably cemented linear

palaeodunes that extend for ~40 km along this coastline. These ridges broadly correspond to the Nahoon Formation of the late Pleistocene Algoa Group, covering the period of marine isotope stages 5 to 2 inclusively [40–42]. Holocene-age dunes in this region, fronting the eroded older dunes, correspond to largely unvegetated foredunes of the Schelm Hoek Formation and are composed of unconsolidated calcareous aeolian sand [43].

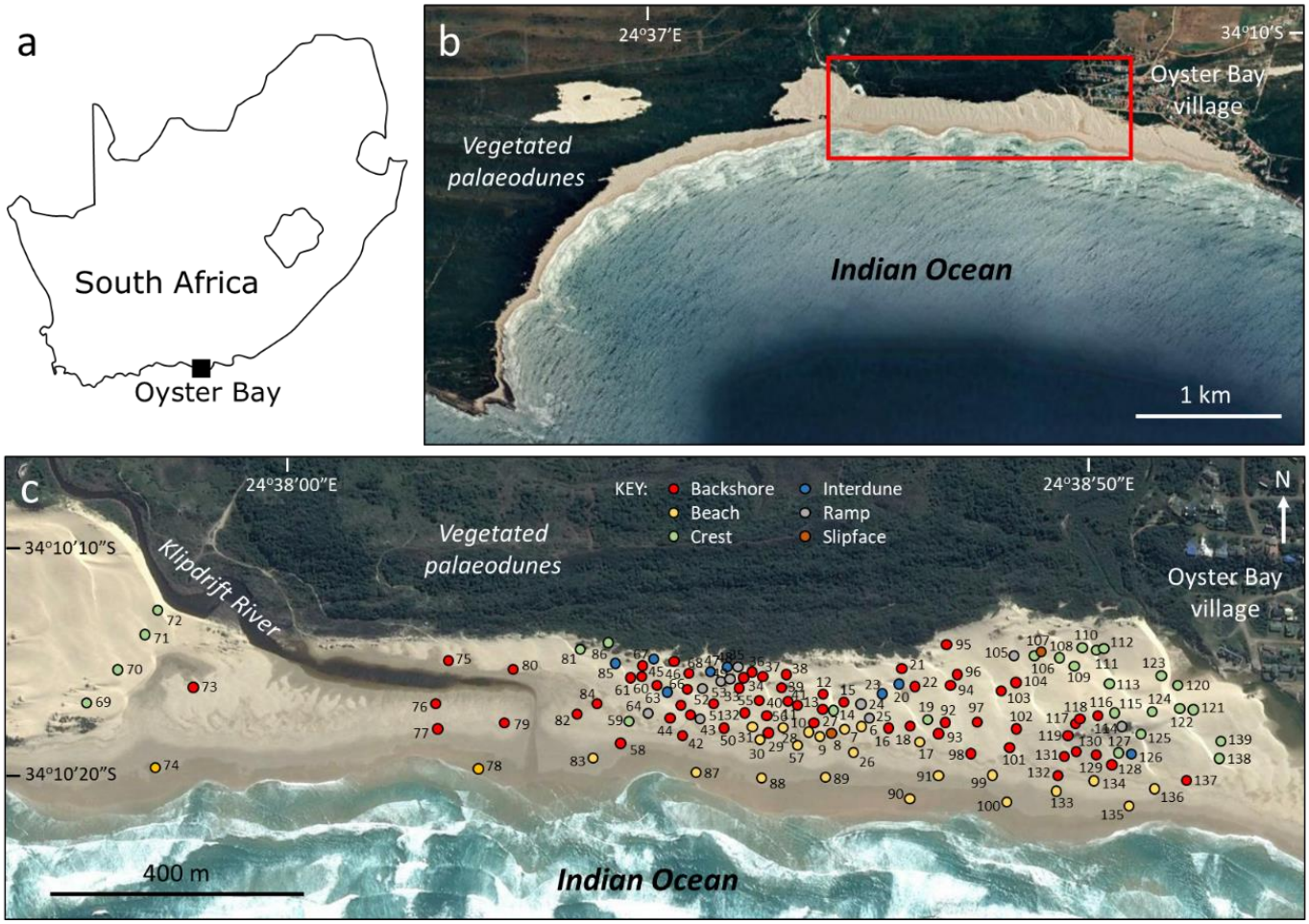

Figure 1. (**a**) Location of the study area at Oyster Bay, Eastern Cape, South Africa; (**b**) large-scale geomorphic setting of Oyster Bay with the sampling region (panel **c**) shown in the red box; (**c**) distribution of sediment sampling points 006–139 (background image in (**c**) from Google Earth, image date 25 August 2013, which is the latest available image before the sampling period).

Surficial (top 5 cm) sediment samples (~400 g each, n = 134, labelled 6–139) were collected in the field across the beach–supratidal dune system in the centre of the Oyster Bay embayment (Figure 1c). A random sampling approach was used but covering the full width of the beach including the intertidal zone. These samples were bagged, labelled, and sampling locations and their geomorphic settings marked using a Garmin Etrex 20 handheld GPS (x y accuracy $\pm$ 3 m). In addition, shells of different species (that were broken and did not contain organisms) were also collected from the intertidal zone. Samples were of the Cape brooding oyster (*Ostrea atherstoni*, sample 1), Brown mussel (*Perna perna*, sample 2), Agulhas ridged nut clam (*Lembulus belcheri*, sample 3), Southern cuttlefish (*Sepia australis*, sample 4), and a mixed shell sample combining these and other shell species found within the intertidal zone (sample 5) (Figure 2). In the laboratory, shell samples (n = 5) were dried and crushed using a pestle and mortar to generate broken fragments >2 mm diameter. Sediment samples were dried, sieved to remove the >2 mm fraction, and a subsample (~50 g) evaluated for $CaCO_3$ content using the loss on ignition method. In this

method, the subsample was weighed, combusted in a muffle furnace for 5 h at 950 °C, and reweighed. Combustible $CaCO_3$ content (% of sample mass) was then calculated. Three replicates were undertaken for each sample, and the results averaged. Variation between the replicates was commonly <0.1%. The grain size distribution for each sample was measured using a Mastersizer 3000 Hydro EV for the size range 0.01–2000 µm with a subsample size of ~5 g. Each subsample was sonificated for 20 s prior to measurement, and five individual grain size distribution patterns were measured using the Mastersizer, and the average taken. The key grain size distribution parameters (D_{10}, D_{50}, D_{90}, kurtosis, skewness, standard deviation and mean) generated by the Mastersizer software were used for analysis. Additionally, a derived parameter herein called *span*, which describes the width of the particle size distribution, was calculated as

$$Span = \frac{(D_{90} - D_{10})}{D_{50}} \quad (1)$$

where D_{90} and D_{10} are the 90th and 10th percentile values of the grain size distribution, and D_{50} is the median grain size.

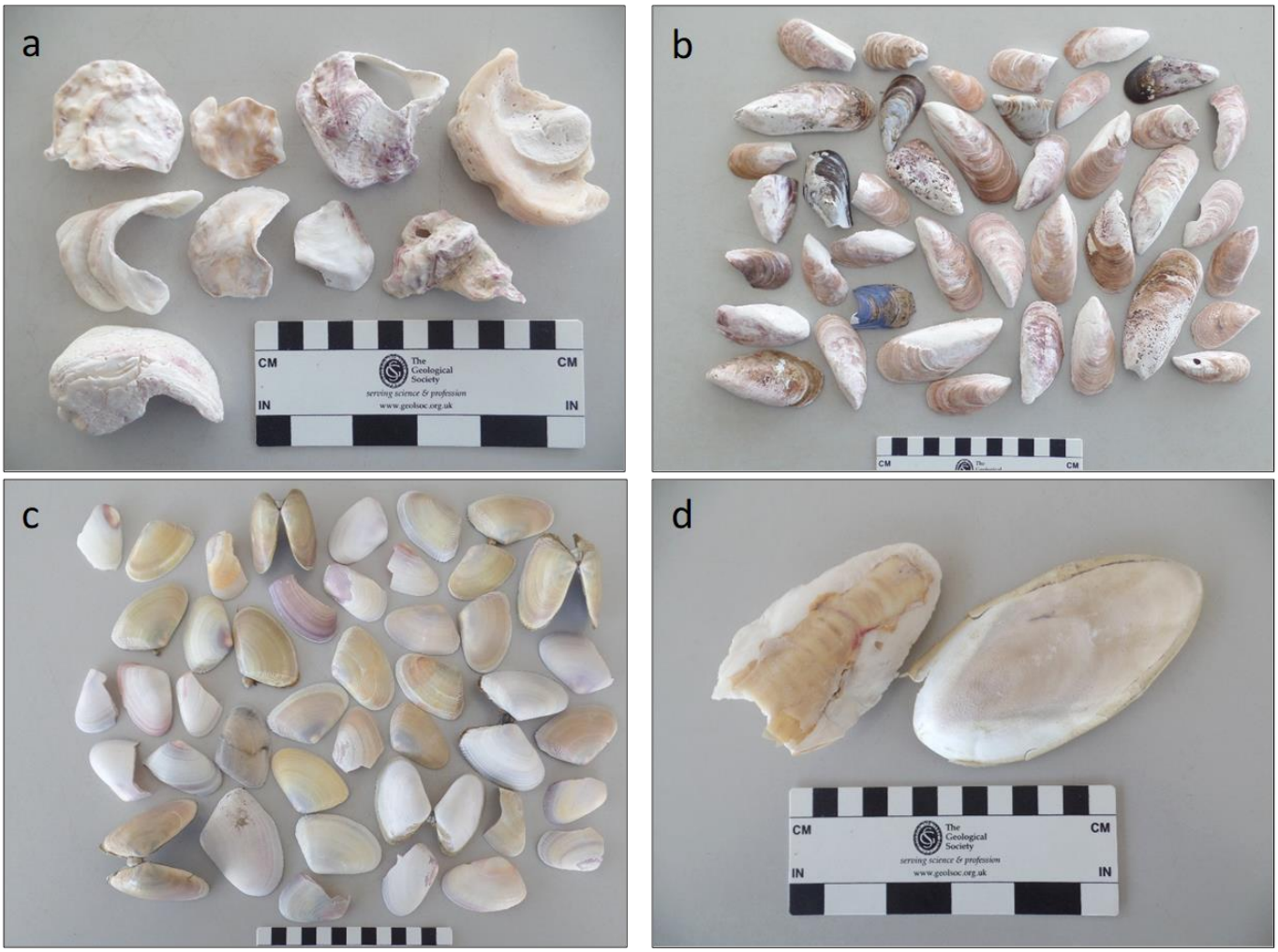

Figure 2. Shell samples collected from Oyster Bay. (**a**) Cape brooding oyster (*Ostrea atherstoni*, sample 1); (**b**) Brown mussel (*Perna perna*, sample 2); (**c**) Agulhas ridged nut clam (*Lembulus belcheri*, sample 3); (**d**) Southern cuttlefish (*Sepia australis*, sample 4).

The spectral signatures of sediment and shell samples were acquired under controlled environmental conditions in the laboratory using an Analytical Spectral Device (ASD)

FieldSpec®3spectrometer (ASD Inc., Boulder, CO, USA) and a light mug (Figure 3). The instrument measures wavelengths from 350 to 2500 nm and compares samples to a white reference panel. The 2 mm-sieved sediment and shell samples were placed in 100 mL glass bottles (Figure 3) and then placed on top of the light mug to measure the reflectance from each sample. Five spectral scans were captured for each sample to ensure spectral stability and an average reflectance was considered for further analysis. The spectrometer was calibrated using the white reference Spectralon® (Figure 3). The spectrometer was recalibrated after every 20 sample scans. The spectral measurement were stored in a notebook computer connected to the device. Figure 3 shows the laboratory setup used in this study.

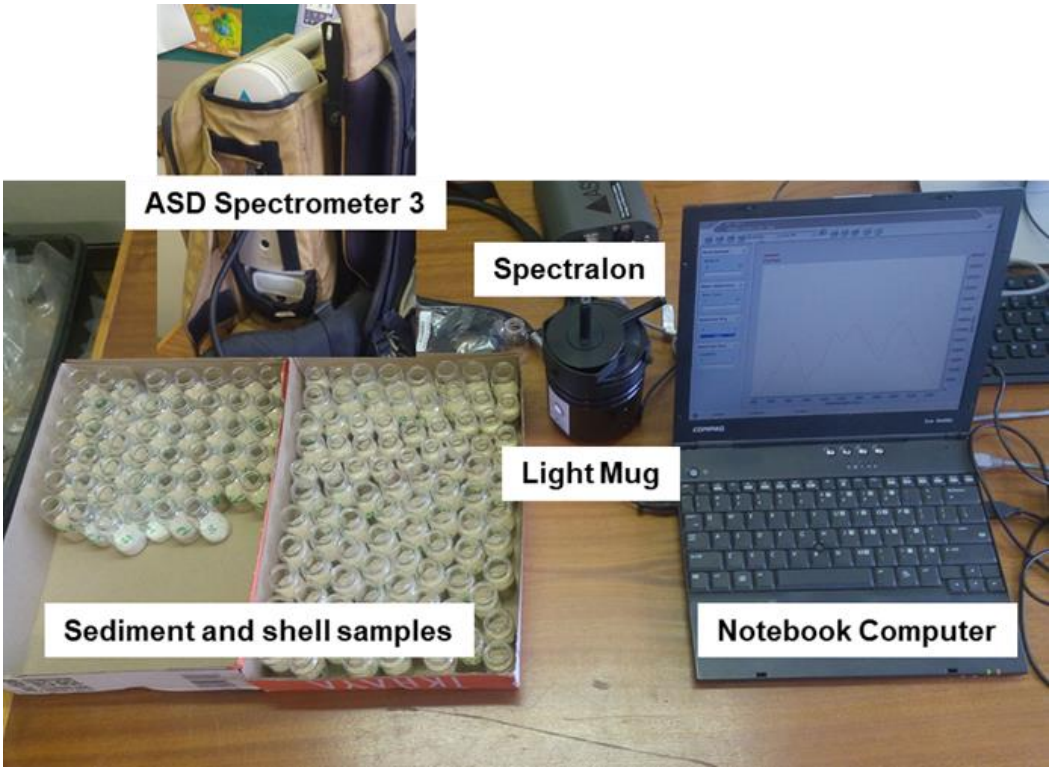

Figure 3. Laboratory spectral measurement system. The system involves an ASD spectroradiometer and a light mug device.

Following ASD data collection, the spectral data were first combined and converted from digital numbers to reflectance values using the ViewSpecPro® software. The spectral resolution was 1 nm which causes several data redundancy difficulties and affects the processing time. The spectral data also went through several pre-processing steps including removing noise-affected spectra located at the edge of the scans. First, the reflectance data less than 375 nm and greater than 2460 nm were removed from further analysis in order to disregard edge effects. Second, the moisture absorption spectral bands (at ~2500, 1950 and 1450 nm; [44]) were therefore eliminated from the final pre-processing stage. A correlation analysis was first performed on the data to identify the spectral wavelengths that show a significant association with different sediment properties. Based on the correlation analysis, specific wavelength regions were then selected. Linear regression analysis and partial least squares regression analysis were then performed on the selected spectral wavelengths based on the magnitude of the correlation coefficient. The data were partitioned into training and testing datasets. Approximately 70% (94 samples) of the dataset was used for the statistical model training, and 30% (40 samples) was used for model testing and validation.

3. Results

3.1. Site Geomorphology and Sediment Dynamics

Oyster Bay contains transgressive transverse dunes within the supratidal part of the beach (Figure 1b), and in the field these are observed to be asymmetric in profile and actively migrating towards the northeast, in the direction of the regional prevailing wind [45] and reflecting the relatively high sediment availability in Oyster Bay. The transgressive dunes show steep slipfaces (Figure 4b) and migrating free dunes over the beach surface (Figure 4c). Older vegetated dunes are left as residual eroded hummocks (Figure 4d).

Figure 4. Dune and beach morphology at Oyster Bay. (**a**) Dissipative beachface within the lower part of the beach system; (**b**,**c**) migrating transverse dune ridges within the supratidal zone; (**d**) erosional hummock of an older vegetated dune system, now isolated within the upper part of the beach.

3.2. Sediment Properties

Detailed laboratory analysis of sediment sample grain size data (Table 1) shows that the samples (n = 134) are remarkably uniform. In terms of texture, samples are dominantly (98%) medium sand with only one sample fine grained and two samples coarse grained. In terms of sorting, most samples (66%) are well sorted, 31% are moderately well sorted and 3% moderately sorted. For skewness, 98% are near symmetrical and 2% are coarse skewed. $CaCO_3$ values vary from 8.22% to 27.29%. For kurtosis, >99% are mesokurtic and only one sample is leptokurtic. The sediment samples were collected from backshore, beach, dune crest, ramp, slipface and interdune positions (Figure 1c). There are some statistically significant differences between grain size end-members (fine and coarse/very coarse sand) and $CaCO_3$ values between some of these sampling positions (Table 2), in particular in beach samples where wave action can contribute to sediment sorting and from supratidal dunes where wind transport leads to effective sediment sorting. As a result, there are some statistical differences between D_{10}, D_{90} and D_{50} values.

Table 1. Details of sediment samples examined in this study. Sample location codes are: BAB: Backshore, beach; BAC: Backshore, crest; BAI: Backshore, interdune; BAR: Backshore, ridge; BAS: Backshore, slipface; BAT: Backshore, trough; BEC: Beach, crest; BEI: Beach, interdune; BER: Beach, ridge; BES: Beach, slipface; BET: Beach, trough; CRI: Crest, interdune; CRR: Crest, ridge; CRS: Crest, slipface; CRT: Crest, trough; INT: Interdune, ridge; INS: Interdune, slipface; INT: Interdune, trough; RAS: Ramp, slipface; RAT: Ramp, trough; SLT: Slipface, trough. Sample numbers are indicated in Figure 1c.

Sample #	Location Code	Lat	Long	Elevation (m asl)	D_{10} (Microns)	D_{50} (Microns)	D_{90} (Microns)	Kurtosis	Skewness	$CaCO_3$ (%)	Fine sand (%)	Medium Sand (%)	Coarse Sand (%)	Very Coarse Sand (%)
006	BEC	−34.171938	24.642923	4.211	209	315	478	0.95	0.00	18.83	24.34	68.06	7.59	0.00
007	BET	−34.171984	24.642668	2.048	220	340	528	0.95	−0.01	13.78	18.57	68.07	13.35	0.00
008	SLT	−34.172052	24.642489	4.932	199	289	421	0.97	0.00	10.40	31.47	65.92	2.61	0.00
009	BES	−34.172016	24.642389	8.777	302	488	804	0.95	−0.02	21.40	3.16	49.36	44.73	2.75
010	BET	−34.172011	24.642128	7.816	226	350	547	0.96	−0.01	13.69	16.50	68.12	15.38	0.00
011	BET	−34.171679	24.641879	5.172	201	323	538	0.98	−0.04	16.20	25.10	61.41	11.89	0.88
012	BEC	−34.171517	24.642276	11.661	204	307	465	0.94	0.00	17.04	26.57	66.99	6.44	0.00
013	BEI	−34.171702	24.642363	11.661	198	288	420	0.97	0.00	9.89	31.79	65.61	2.60	0.00
014	CRS	−34.171690	24.642476	9.739	279	442	715	0.96	−0.02	21.98	5.30	57.36	36.33	1.01
015	SLT	−34.171666	24.642576	8.296	203	303	453	0.95	−0.01	12.30	27.39	67.18	5.43	0.00
016	BET	−34.171933	24.643384	6.134	220	340	529	0.95	−0.01	14.58	18.69	67.89	13.42	0.00
017	BEC	−34.172137	24.643902	9.739	254	392	609	0.96	−0.01	19.09	9.01	66.63	24.29	0.06
018	BEC	−34.171929	24.643805	7.816	207	311	470	0.95	−0.01	16.44	25.28	67.90	6.82	0.00
019	CRS	−34.171833	24.644029	12.382	248	382	589	0.95	−0.01	16.60	10.45	67.69	21.83	0.03
020	BET	−34.171374	24.643891	5.893	189	287	440	0.96	−0.01	12.66	34.09	61.50	4.41	0.00
021	BEC	−34.171120	24.643643	9.017	214	321	485	0.96	0.00	19.35	22.28	69.53	8.19	0.00
022	INR	−34.171363	24.643649	7.095	228	374	631	0.96	−0.03	18.76	15.15	60.88	23.40	0.50
023	INR	−34.171499	24.643289	9.498	217	351	583	0.97	−0.04	16.97	18.85	62.41	17.85	0.56
024	RAS	−34.171600	24.642989	9.979	218	343	543	0.96	−0.01	16.90	19.06	66.14	14.79	0.00
025	RAS	−34.171869	24.643010	6.134	204	318	503	0.95	−0.02	12.93	25.10	64.54	10.36	0.00
026	BAB	−34.172203	24.642861	8.537	199	302	459	0.95	−0.01	16.21	28.53	65.40	6.06	0.00

Table 1. *Cont.*

Sample #	Location Code	Lat	Long	Elevation (m asl)	D_{10} (Microns)	D_{50} (Microns)	D_{90} (Microns)	Kurtosis	Skewness	$CaCO_3$ (%)	Fine sand (%)	Medium Sand (%)	Coarse Sand (%)	Very Coarse Sand (%)
027	BAT	−34.171951	24.642091	1.087	219	339	528	0.95	−0.01	16.78	19.19	67.50	13.30	0.00
028	BAT	−34.171980	24.641696	6.134	226	372	631	0.97	−0.03	21.13	15.64	60.75	22.84	0.70
029	BAC	−34.171961	24.641441	7.095	211	314	472	0.95	0.00	14.73	23.86	69.23	6.91	0.00
030	BAT	−34.171942	24.641264	5.893	200	311	490	0.96	−0.02	13.61	26.92	64.19	8.89	0.00
031	BEC	−34.171955	24.641151	5.653	221	344	530	0.95	0.01	19.22	18.14	68.19	13.67	0.00
032	BES	−34.171565	24.641033	6.134	261	416	669	0.95	−0.01	20.08	7.88	60.64	30.94	0.54
033	BEC	−34.171277	24.640809	3.250	187	274	402	0.95	0.00	22.41	38.30	59.87	1.83	0.00
034	BAT	−34.171125	24.640865	8.296	202	307	466	0.95	0.00	17.58	27.05	66.48	6.47	0.00
035	RAS	−34.171038	24.640841	7.816	219	336	514	0.95	0.00	12.13	19.35	68.71	11.94	0.00
036	BAC	−34.171123	24.640999	5.653	210	316	481	0.96	0.00	20.16	23.92	68.25	7.83	0.00
037	BAT	−34.171193	24.641281	0.125	254	466	1020	1.06	−0.13	26.58	9.31	46.06	34.29	8.86
038	BAC	−34.171223	24.641788	4.692	191	284	425	0.96	0.00	19.23	34.60	62.35	3.04	0.00
039	BAR	−34.171376	24.641656	6.374	180	264	388	0.96	−0.01	12.38	42.81	55.96	1.22	0.00
040	BAT	−34.171621	24.641768	4.451	213	327	508	0.95	−0.01	14.72	21.97	67.04	11.00	0.00
041	BAC	−34.171713	24.641632	7.335	239	366	565	0.95	−0.01	18.44	13.12	68.71	18.16	0.00
042	BAB	−34.172004	24.639971	1.808	225	363	589	0.95	−0.01	14.92	16.26	63.45	20.20	0.09
043	BAC	−34.171775	24.639973	6.854	235	340	488	0.95	0.02	18.42	14.63	77.03	8.34	0.00
044	BAC	−34.171648	24.639890	9.258	219	328	494	0.96	−0.01	15.84	19.78	71.01	9.20	0.00
045	BAS	−34.171388	24.639973	8.296	253	393	611	0.96	−0.01	19.06	9.30	66.09	24.55	0.06
046	BAC	−34.171020	24.639773	10.700	213	322	490	0.96	0.00	19.00	22.25	68.96	8.79	0.00
047	BAS	−34.171247	24.640023	5.413	203	310	481	0.96	−0.02	10.27	26.40	65.66	7.94	0.00
048	RAT	−34.171330	24.640202	6.374	206	318	495	0.95	−0.01	15.96	24.55	66.09	9.36	0.00
049	RAS	−34.171756	24.640200	6.134	239	391	671	0.97	−0.05	17.20	12.77	59.31	26.55	1.37
050	BAC	−34.171887	24.640709	5.653	222	350	556	0.96	−0.01	17.06	17.60	66.07	16.32	0.01

Table 1. *Cont.*

Sample #	Location Code	Lat	Long	Elevation (m asl)	D_{10} (Microns)	D_{50} (Microns)	D_{90} (Microns)	Kurtosis	Skewness	$CaCO_3$ (%)	Fine sand (%)	Medium Sand (%)	Coarse Sand (%)	Very Coarse Sand (%)
051	BAC	−34.171602	24.640481	3.730	217	359	625	0.99	−0.06	20.63	18.40	59.74	20.10	1.31
052	RAT	−34.171232	24.640564	3.971	176	248	347	0.96	−0.01	15.27	51.21	48.62	0.17	0.00
053	RAT	−34.171263	24.640642	7.816	192	274	391	0.96	0.00	16.61	37.27	61.61	1.12	0.00
054	INT	−34.171117	24.640536	6.374	201	300	448	0.96	0.00	15.57	28.33	66.84	4.84	0.00
055	BAT	−34.171473	24.641231	5.893	207	319	498	0.95	−0.01	14.82	24.19	66.06	9.75	0.00
056	BAT	−34.171814	24.641265	7.335	205	326	530	0.95	−0.03	14.89	23.92	62.98	13.00	0.07
057	BAB	−34.172157	24.641878	3.730	197	289	427	0.97	0.00	13.48	31.65	65.29	3.06	0.00
058	BAB	−34.171930	24.639000	6.374	226	350	549	0.96	−0.01	15.02	16.61	67.71	15.67	0.00
059	CRI	−34.171679	24.639045	7.576	207	306	454	0.95	−0.01	17.67	26.14	68.32	5.54	0.00
060	BAC	−34.171248	24.639070	8.537	214	344	568	0.96	−0.03	20.12	20.34	62.49	17.06	0.11
061	BAC	−34.171124	24.639230	6.374	243	443	1240	1.09	−0.25	24.65	11.32	46.87	27.58	11.11
062	BAT	−34.171242	24.639314	0.606	195	291	438	0.96	−0.01	9.97	31.81	64.08	4.11	0.00
063	MAI	−34.171381	24.639556	5.893	219	345	551	0.96	−0.02	17.32	18.71	65.64	15.63	0.01
064	RAT	−34.171685	24.639376	4.451	217	354	620	1.00	−0.07	19.63	18.90	60.14	18.94	1.53
065	BAT	−34.171786	24.639684	7.816	216	329	504	0.96	0.00	16.76	20.70	68.83	10.47	0.00
066	INT	−34.171465	24.639731	3.730	214	351	616	0.99	−0.07	15.92	19.78	59.69	18.78	1.41
067	INR	−34.170996	24.639434	13.103	208	324	510	0.95	−0.01	18.77	23.52	65.21	11.27	0.00
068	INS	−34.171154	24.640406	8.777	219	327	488	0.96	0.00	18.75	19.95	71.52	8.53	0.00
069	CRI	−34.171594	24.629845	−5.641	238	406	722	0.98	−0.04	23.67	12.58	55.56	29.39	2.34
070	CRI	−34.171147	24.630392	12.863	246	396	639	0.96	0.00	18.05	11.02	61.88	26.90	0.21
071	CRI	−34.170616	24.630827	12.622	252	388	594	0.96	0.00	19.25	6.45	67.59	22.95	0.01
072	CRS	−34.170290	24.631101	10.700	262	392	583	0.95	0.00	19.47	7.53	70.20	22.27	0.01
073	BAR	−34.171394	24.631663	8.296	195	302	474	0.96	−0.02	18.67	29.59	6.97	7.43	0.00
074	BER	−34.172438	24.631051	−0.354	223	334	498	0.96	0.00	14.11	18.15	72.14	9.72	0.00

Table 1. *Cont.*

Sample #	Location Code	Lat	Long	Elevation (m asl)	D_{10} (Microns)	D_{50} (Microns)	D_{90} (Microns)	Kurtosis	Skewness	$CaCO_3$ (%)	Fine sand (%)	Medium Sand (%)	Coarse Sand (%)	Very Coarse Sand (%)
075	BAR	−34.170938	24.635953	6.134	220	358	581	0.95	0.00	22.10	17.65	62.85	19.47	0.03
076	BAT	−34.171616	24.635743	10.459	196	287	423	0.97	0.00	11.41	32.60	64.59	2.81	0.00
077	BAC	−34.171935	24.635784	4.692	215	331	512	0.95	−0.01	17.54	20.85	67.59	11.56	0.00
078	BER	−34.172500	24.636502	5.653	219	337	521	0.95	−0.01	14.71	19.23	68.12	12.65	0.00
079	BAT	−34.171834	24.636919	8.537	241	361	545	0.96	−0.01	13.34	12.68	71.64	15.68	0.00
080	BAR	−34.171110	24.637048	8.777	213	343	562	0.96	−0.02	20.47	20.49	62.92	16.54	0.05
081	CRS	−34.170847	24.638189	13.584	253	432	808	0.99	−0.08	27.25	9.38	53.07	33.00	4.49
082	BAB	−34.171690	24.638149	4.932	234	354	530	0.94	0.01	15.92	14.35	71.73	13.92	0.00
083	BAB	−34.172336	24.638428	7.335	239	429	865	0.99	−0.10	25.33	12.28	49.43	31.89	6.09
084	BAI	−34.171595	24.638524	2.048	197	294	442	0.96	−0.01	20.45	30.71	64.88	4.41	0.00
085	INR	−34.171029	24.638807	10.459	236	371	584	0.94	−0.01	20.34	13.49	65.94	20.54	0.04
086	CRI	−34.170733	24.638722	13.584	190	275	396	0.96	0.00	15.50	37.34	61.22	1.44	0.00
087	BET	−34.172485	24.640166	5.413	196	281	400	0.96	0.00	12.29	34.09	64.39	1.51	0.00
088	BET	−34.172541	24.641305	5.653	234	385	642	0.95	−0.01	19.48	13.60	60.30	25.74	0.36
089	BET	−34.172570	24.642399	1.567	275	436	699	0.95	−0.01	19.73	5.96	58.23	35.16	0.65
090	BET	−34.172851	24.643780	5.893	336	517	801	0.96	−0.01	24.00	1.02	45.16	51.74	2.09
091	BAB	−34.172520	24.644298	4.451	204	296	430	0.96	0.00	12.54	28.48	68.45	3.07	0.00
092	BAS	−34.172002	24.644281	6.134	193	272	385	0.96	0.00	8.26	37.81	61.32	0.87	0.00
093	BAS	−34.171981	24.644318	7.335	200	297	443	0.96	−0.01	8.86	29.30	66.25	4.45	0.00
094	BAC	−34.171375	24.644495	9.739	256	403	643	0.96	−0.01	17.99	8.82	63.06	27.87	0.25
095	BAR	−34.170761	24.644425	8.296	224	338	511	0.96	−0.01	17.33	17.64	70.80	11.57	0.00
096	BAT	−34.171188	24.644581	6.614	215	338	553	0.97	−0.04	13.67	20.53	64.14	14.33	0.54
097	BAI	−34.171828	24.644937	7.816	213	330	518	0.95	−0.01	13.86	21.65	66.14	12.21	0.00
098	BAT	−34.172261	24.644822	5.413	201	289	416	0.96	0.00	8.22	30.99	66.75	2.26	0.00

Table 1. *Cont.*

Sample #	Location Code	Lat	Long	Elevation (m asl)	D_{10} (Microns)	D_{50} (Microns)	D_{90} (Microns)	Kurtosis	Skewness	$CaCO_3$ (%)	Fine sand (%)	Medium Sand (%)	Coarse Sand (%)	Very Coarse Sand (%)
099	BAB	−34.172608	24.645214	6.134	217	329	504	0.96	−0.01	14.48	20.40	69.15	10.46	0.00
100	BER	−34.172899	24.645462	4.451	249	375	565	0.96	0.00	13.02	10.23	71.10	18.67	0.00
101	BAC	−34.172244	24.645432	8.056	235	353	535	0.95	−0.01	18.51	14.37	71.23	14.40	0.00
102	BAC	−34.171919	24.645569	9.258	225	349	541	0.96	0.00	21.15	16.78	68.35	14.88	0.00
103	BAS	−34.171447	24.645305	10.700	294	479	796	0.96	−0.02	22.23	3.75	50.59	42.96	2.71
104	BAT	−34.171306	24.645469	7.576	227	355	564	0.96	−0.02	14.56	16.22	66.43	17.32	0.02
105	RAS	-34.296997	24.645517	10.700	219	340	532	0.95	−0.01	18.10	18.95	67.40	13.65	0.00
106	CRS	−34.170927	24.645926	10.459	250	444	1030	1.11	−0.19	24.17	9.93	48.97	30.52	8.51
107	SLT	−34.170939	24.645957	9.498	214	314	460	0.95	0.00	10.60	22.94	71.26	5.80	0.00
108	CRR	−34.170890	24.646282	10.459	229	361	571	0.96	0.00	17.58	15.24	66.17	18.57	0.02
109	CRR	−34.171110	24.646571	11.901	218	351	573	0.96	−0.01	20.53	18.70	63.19	18.05	0.05
110	CRT	−34.170858	24.646711	7.335	195	293	442	0.96	0.00	12.43	31.15	64.41	4.41	0.00
111	CRS	−34.170820	24.646927	9.258	250	392	625	0.97	−0.02	20.51	10.04	64.54	25.21	0.21
112	CRT	−34.170819	24.647034	4.451	209	322	503	0.95	−0.01	11.89	23.57	66.05	10.37	0.00
113	CRR	−34.171350	24.647209	13.103	213	316	469	0.95	0.00	16.22	22.98	70.41	6.61	0.00
114	RAS	−34.171908	24.647452	19.832	179	265	391	0.95	0.00	12.67	42.77	55.89	1.34	0.00
115	CRR	−34.171724	24.647273	21.995	190	272	388	0.96	0.00	16.95	38.57	60.42	1.00	0.00
116	BAC	−34.171782	24.646935	20.313	204	308	467	0.95	−0.01	20.51	26.57	66.85	6.58	0.00
117	BAS	−34.171910	24.646599	12.622	200	295	437	0.96	0.00	12.42	29.66	66.46	3.88	0.00
118	BAC	−34.171930	24.646544	17.910	220	327	489	0.96	0.00	18.03	19.74	71.69	8.57	0.00
119	BAC	−34.172095	24.646437	12.622	244	372	571	0.96	−0.01	19.95	11.50	69.24	19.25	0.01
120	CRS	−34.171342	24.648271	4.451	197	280	393	0.96	0.00	8.99	34.25	64.66	1.09	0.00
121	CRS	−34.171682	24.648521	11.421	202	309	476	0.95	−0.01	13.09	26.68	65.85	7.47	0.00
122	CRS	−34.171691	24.648334	13.824	203	288	407	0.96	0.00	16.36	30.69	67.61	1.70	0.00

Table 1. *Cont.*

Sample #	Location Code	Lat	Long	Elevation (m asl)	D_{10} (Microns)	D_{50} (Microns)	D_{90} (Microns)	Kurtosis	Skewness	$CaCO_3$ (%)	Fine sand (%)	Medium Sand (%)	Coarse Sand (%)	Very Coarse Sand (%)
123	CRS	−34.171218	24.648048	13.103	266	422	678	0.94	−0.01	19.95	7.19	60.04	32.25	0.53
124	CRS	−34.171781	24.647969	22.716	189	264	372	0.96	0.01	19.57	41.90	57.63	0.47	0.00
125	CRS	−34.172032	24.647721	16.948	188	263	371	0.96	0.01	12.07	42.40	57.15	0.45	0.00
126	INR	−34.172320	24.647587	12.863	201	295	432	0.96	0.00	11.01	29.49	67.17	3.34	0.00
127	CRS	−34.172309	24.647358	16.468	301	466	733	0.96	−0.02	20.23	2.83	54.98	41.19	1.09
128	BAT	−34.172380	24.647111	9.979	214	330	512	0.95	−0.01	13.46	21.34	67.11	11.56	0.00
129	BAC	−34.172293	24.646948	12.382	213	313	458	0.95	0.00	17.74	23.50	70.80	5.70	0.00
130	BAT	−34.172286	24.646591	10.940	217	325	488	0.96	0.00	14.41	20.83	70.66	8.52	0.00
131	BAC	−34.172367	24.646384	10.459	212	317	478	0.96	0.00	14.05	23.17	69.29	7.54	0.00
132	BAB	−34.172595	24.646253	4.932	220	330	497	0.96	0.00	12.53	19.34	71.00	9.66	0.00
133	BAB	−34.172955	24.646132	6.854	285	500	941	0.96	−0.06	27.29	5.15	44.90	41.99	7.86
134	BAB	−34.172679	24.646923	4.692	208	312	471	0.95	−0.01	14.71	25.00	68.10	6.90	0.00
135	BER	−34.173066	24.647486	6.614	250	373	558	0.96	0.00	14.17	10.10	72.04	17.87	0.00
136	BAB	−34.172787	24.647920	5.172	216	316	463	0.96	0.00	13.70	22.17	71.79	6.04	0.00
137	BAT	−34.172667	24.648487	3.490	221	331	494	0.96	0.00	14.50	18.94	71.83	9.24	0.00
138	CRS	−34.172431	24.648988	6.614	229	333	485	0.96	0.00	16.86	16.69	75.25	8.06	0.00
139	CRT	−34.172160	24.649022	4.451	210	293	408	0.97	0.01	13.16	27.66	70.87	1.48	0.00

Table 2. Table of *p*-values obtained for different sediment properties from different sampling locations (Table 1), analysed using Fisher's partial least squares discriminant analysis. Significance levels are: ^ 0.1, * 0.05, ** 0.01 and *** 0.001.

Location	D_{10}	D_{50}	D_{90}	$CaCO_3$	Fine Sand	Medium Sand	Coarse Sand	Very Coarse Sand
Backshore, beach	0.0002 ***	0.0004 ***	0.0041 **	0.0455 *	0.0120 *	0.2313	0.0003 **	0.0148 *
Backshore, crest	0.0265 *	0.0318 *	0.0475 *	0.0005 **	0.1433	0.9129	0.0221 *	0.1460
Backshore, interdune	0.8668 ^	0.5823	0.5154	0.9509	0.7269	0.8188	0.3936	0.8481
Backshore, ramp	0.1903	0.3554	0.6308	0.9566	0.0472 *	0.5359	0.7108	0.9965
Backshore, slip face	0.4271	0.4077	0.5417	0.0813 ^	0.2634	0.7330	0.4244	0.9953
Backshore, trough	0.4534	0.8241	0.7296	0.0782 ^	0.3678	0.8872	0.9339	0.4140
Beach, crest	0.0113 *	0.0144 *	0.0817 ^	0.5547	0.0814 ^	0.1914	0.0192 *	0.0967 ^
Beach, interdune	0.0038 **	0.0141 *	0.0757 ^	0.1113	0.0803 ^	0.2343	0.0283 *	0.0674 ^
Beach, ramp	<0.0001 ***	<0.0001 ***	0.0022 *	0.0705 ^	<0.0001 ***	0.5811	0.0003 **	0.0241 *
Beach, slip face	0.0069 **	0.0076 **	0.0365 *	0.0067 **	0.0172 *	0.3404	0.0081 *	0.1989
Beach, trough	<0.0001 *	<0.0001 ***	0.0032 **	0.0002 ***	0.0004 **	0.1425	<0.0001 ***	0.0379 *
Crest, interdune	0.1626	0.3588	0.4935	0.0148 *	0.5158	0.7372	0.4968	0.4123
Crest, ramp	0.0007 ***	0.0036 **	0.0235 *	0.0031 **	0.0004 **	0.5245	0.0163 *	0.2081
Crest, slip face	0.0879 ^	0.0868 ^	0.1549	0.0015 **	0.0819 ^	0.6903	0.0820 ^	0.5586
Crest, trough	0.0001 ***	0.0019 **	0.0328 *	<0.0001 ***	0.0018 **	0.7333	0.0039 *	0.4294
Interdune, ramp	0.2232	0.2070	0.3184	0.9891	0.0532 ^	0.4740	0.2720	0.8547
Interdune, slip face	0.4023	0.2783	0.3484	0.0957 ^	0.2141	0.8496	0.2197	0.9095
Interdune, trough	0.4658	0.4445	0.6438	0.1765	0.2997	0.8822	0.3813	0.7004
Ramp, slip face	0.9154	0.7360	0.7257	0.0839 ^	0.9405	0.5169	0.5545	0.9972
Ramp, trough	0.4020	0.3912	0.3970	0.1098	0.1386	0.4083	0.6216	0.4729
Slip face, trough	0.6099	0.4454	0.4397	0.2822	0.4334	0.7691	0.3904	0.7306

Analysis of the covariation between different sediment properties shows that there are statistically significant relationships between several property types (Table 3). The properties that refer specifically to dimensional values of the grain size distribution (D_{10}, D_{50} and D_{90}) show evidence for very high correlation coefficients (<0.95) which is indicative of autocorrelation. Dimensionless parameters of skewness and kurtosis show more variable relationships but are also relatively strongly correlated (both positively and negatively) with grain size variables. The nondimensional parameter *span* broadly expresses the distributional range of particle sizes within the sample (Equation (1)) and thus has a high correlation coefficient with distributional parameters (Table 3). The independent parameter of $CaCO_3$ content shows a strong positive (negative) relationship with coarse (fine) sand because of the mechanical break up of marine shells over time, forming relatively large shell fragments mixed in with coarse mineral sand [46].

Averaged spectral characterisation of sediment samples from different geomorphic positions at Oyster Bay are presented in Figure 5. There are generally similar patterns seen at all positions, consistent with their generally similar sediment grain size compositions (Table 2), with some consistent variability in the water absorption bands. There is greatest variability in particular within the SWIR at ~1850–2400 nm. It is also notable that beach samples show somewhat more variability than samples from other positions, with higher reflectance values (compared to other positions) in the VNIR and lower values in the SWIR (Figure 5a). Based on the high correlation coefficients of beach samples with fine sand and $CaCO_3$ values (Table 2), we therefore speculate that this spectral variability of beach samples reflects the disproportionate influence of fine sand and $CaCO_3$ from shell fragments within these samples. The nature of these samples are now explored in more detail.

Table 3. Pearson Product Moment Correlation of different sediment properties across all samples (n = 134). F = fine, M = medium, C = coarse and VC = very coarse. Variable *span* is defined in the text. Significance levels are: ^ 0.1, * 0.05, ** 0.01 and *** 0.001.

	D_{10}	D_{50}	D_{90}	Kurtosis	Skewness	$CaCO_3$	F Sand	M Sand	C Sand	VC Sand
D_{10}	1.000									
D_{50}	0.951 ***	1.000								
D_{90}	0.754 ***	0.903 ***	1.000 ***							
Kurtosis	0.139	0.318 ***	0.634 ***	1.000						
Skewness	−0.252 **	−0.477 ***	−0.793 ***	−0.890 ***	1.000					
$CaCO_3$	0.571 ***	0.679 ***	0.698 ***	0.337 ***	−0.463 ***	1.000				
F sand	−0.914 ***	−0.918 ***	−0.761 ***	−0.156 ^	0.300 ***	−0.557 ***	1.000			
M sand	−0.201 *	−0.332 ***	−0.451 ***	−0.383 ***	0.478 ***	−0.411 ***	0.030	1.000		
C sand	0.928 ***	0.984 ***	0.872 ***	0.266 **	−0.443 ***	0.679 ***	−0.880 ***	−0.393 ***	1.000	
VC sand	0.414 ***	0.603 ***	0.853 ***	0.813 ***	−0.895 ***	0.566 ***	−0.367 ***	−0.529 ***	0.545 ***	1.000
Span	0.403 ***	0.642 ***	0.902 ***	0.782 ***	−0.941 ***	0.593 ***	−0.493 ***	−0.469 ***	0.616 ***	0.885 ***

3.3. Spectral Analysis of Sediment Samples

The spectral variation at the VNIR and SWIR bands can be examined in detail using the correlation matrices between selected sample particle size characteristics and $CaCO_3$ content. Here, we systematically calculate the correlation coefficient of D_{10}, $CaCO_3$, D_{90}, fine sand and kurtosis at 1 nm wavelength increments through the NVIR and SWIR wavebands (Figure 6). This shows that certain parts of the spectrum are associated with greater (positive or negative) correlation coefficient values and thus are more useful in terms of discriminating between different sediment properties at those wavelengths. For example, in the range ~700–1350 nm there is a clear discrimination between high positive correlations for D_{10} and D_{90} and high negative correlation for fine sand (Figure 6). Here, kurtosis and $CaCO_3$ shows no correlation. Likewise, in the range ~1850–2450 nm there is greater statistical discrimination between fine sand (highest positive correlation) and $CaCO_3$ (highest negative correlation) values. By contrast, the region ~1450–1700 nm is not useful for discriminating any sediment properties, because there are very low correlation coefficients throughout (i.e., all correlation coefficients are around zero).

The statistical relationships of $CaCO_3$ values, fine sand and grain size *span* to different wavelengths are described in Table 4, which shows the outputs of a linear regression model for each variable. The results highlight that certain wavelengths have a statistically significant relationship to some sediment properties. For example, $CaCO_3$ shows greatest significance in the wavelength range ~1052–1252 nm, which falls within the VNIR part of the spectrum. Fine sand has the greatest significance at shorter VNIR wavelengths (~852–952 nm), and *span* shows significance in isolated parts of the spectrum (2300, 2400 and 2447 nm) at the end of the SWIR range, which may be an artefact of sediment composition within the sample as a whole, e.g., [47]. Water absorption at the 1352 nm waveband has a strong signal and therefore this waveband is removed from the analysis (Table 4) in order to avoid erroneous overfitting.

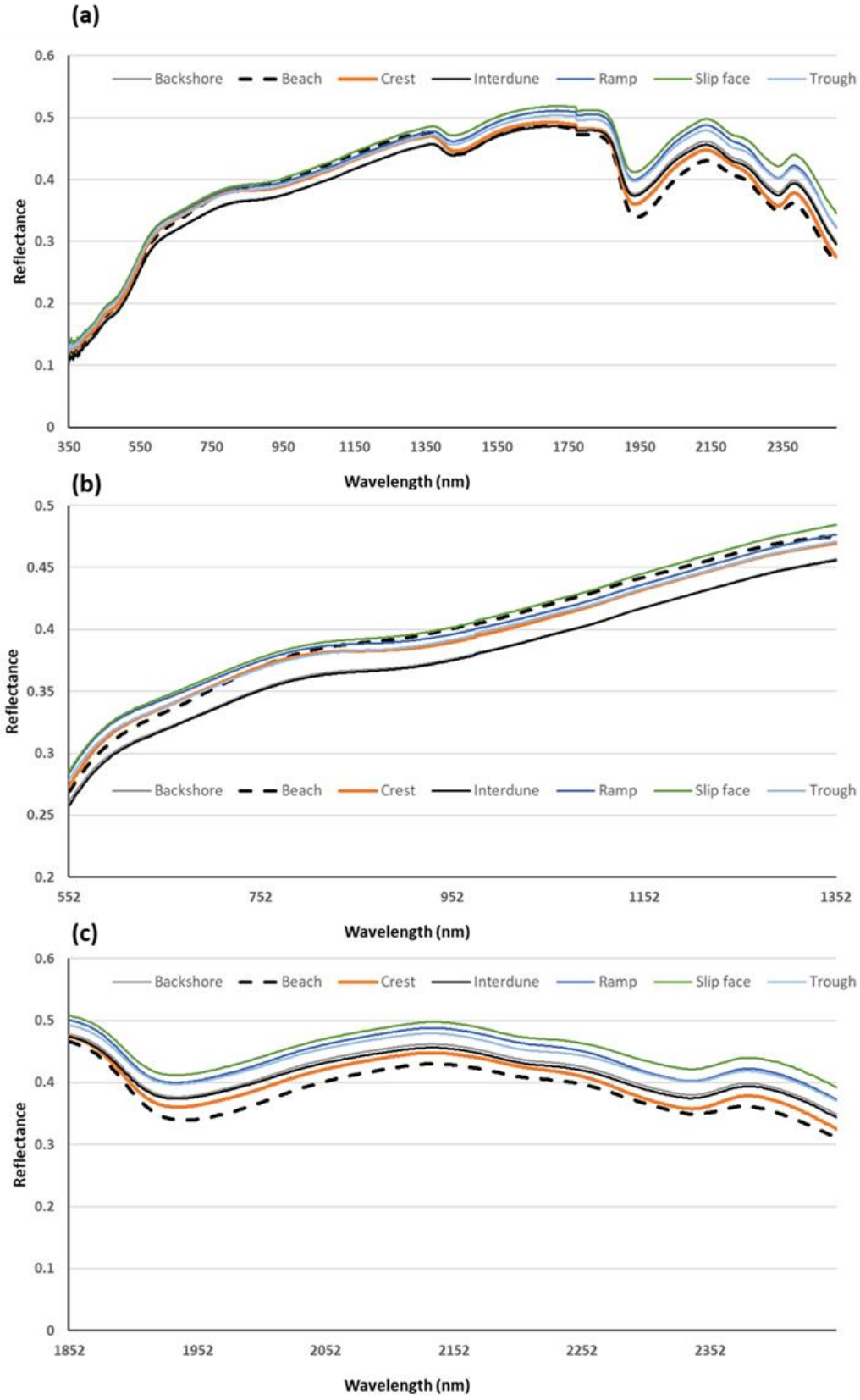

Figure 5. Results of spectral analysis of samples from different geomorphic positions at Oyster Bay. (**a**) Full average spectrum for samples from the different position; detailed results at (**b**) the VNIR (552–1352 nm) and (**c**) SWIR (1852–2450 nm) parts of the spectrum.

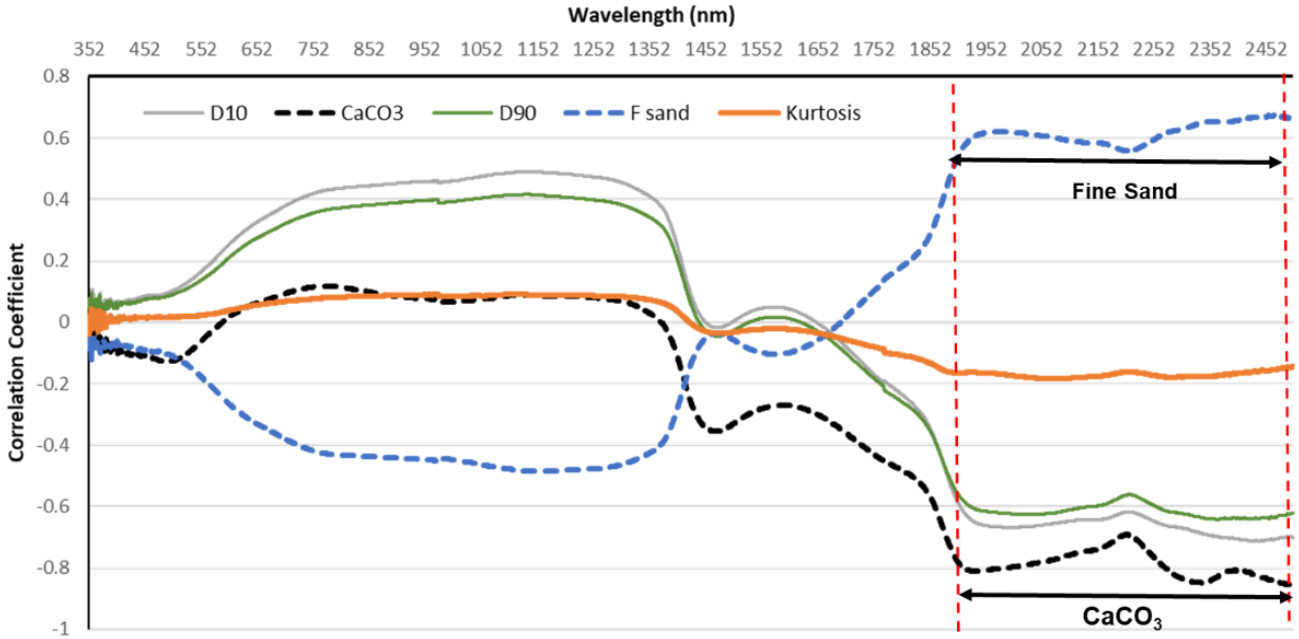

Figure 6. Correlation coefficient between reflectance values at different spectral wavelengths and sediment $CaCO_3$, and particle size characteristics.

Table 4. Analysis of *p*-values of linear regression of $CaCO_3$, fine sand and grain size *span* with selected wavelengths (see Figure 5). Significance levels are: ^ 0.1, * 0.05, ** 0.01 and *** 0.001.

Wavelength (nm)	$CaCO_3$	Fine Sand	Span
552	0.0928 ^	0.6264	0.9885
652	0.2507	0.9883	0.4891
752	0.7211	0.0928 ^	0.0734 ^
852	0.7343	0.0096 **	0.1257
952	0.9410	0.0026 **	0.2164
1052	0.0077 **	0.7944	0.3640
1152	0.0100 *	0.9415	0.2201
1252	0.0087 **	0.4923	0.1494
1462	0.0834 ^	0.2163	0.3150
1552	0.3162	0.8246	0.2073
1652	0.2605	0.9801	0.1364
1752	0.1525	0.8957	0.1300
1789	0.1064	0.0480 *	0.0158 *
1962	0.0264 *	0.7977	0.0528 ^
2028	0.4413	0.4095	0.2356
2082	0.9618	0.5296	0.6334
2152	0.4212	0.4293	0.7909
2200	0.5897	0.5675	0.6655
2252	0.3046	0.0789 ^	0.3075
2300	0.0098 **	0.4795	0.0085 **
2335	0.1032	0.8612	0.8394

Table 4. *Cont.*

Wavelength (nm)	$CaCO_3$	Fine Sand	Span
2338	0.1530	0.8069	0.7031
2350	0.7137	0.0696 ˆ	0.4356
2352	0.2443	0.0253 *	0.9282
2370	0.3290	0.2500	0.7780
2400	0.3596	0.3150	0.0041 **
2420	0.3237	0.1892	0.2231
2435	0.2855	0.0127 *	0.7258
2447	0.6500	0.0760 ˆ	0.0024 **
2450	0.2281	0.0470 *	0.5175
Adjusted R^2	0.8978	0.7510	0.5510
Overall *p*-value	2.2×10^{-16} ***	2×10^{-16} ***	4.88×10^{-16} ***

$CaCO_3$ values can be estimated using single wavelength relationships as:

$$CaCO_3 = 54.1 - 98.37R_{2335} \left(R^2 = 0.718,\ n = 94\right) \quad (2)$$

where R_{2335} is reflectance at the 2335 nm wavelength. A similar model performance can be achieved at the wavelength between 2038 and 2435 nm. A multilinear relationship can improve the model estimation as follows:

$$CaCO_3 = 38.99 + 460.23R_{2200} - 1272.89R_{2300} + 1158.99R_{2335} - 409.99R_{2370} \left(R^2 = 0.872,\ n = 94\right) \quad (3)$$

where R_{2200}, R_{2300}, R_{2335}, R_{2335}, and R_{2335} are reflectances at the 2200, 2300, 2335 and 2370 nm wavelengths, respectively. Fine sand can be estimated using the following linear relationship:

$$F\ Sand = 179.06R_{2450} - 41.01 \left(R^2 = 0.463,\ n = 94\right) \quad (4)$$

where *F Sand* is the fine sand percentage, and R_{2450} is reflectance at the 2450 nm wavelength. Fine sand values can also be estimated using the reflectance from the wavelengths ranging between 552 and 1789 nm. This can also be used to develop an improved model to estimate the fine sand percentage as follows:

$$F\ Sand = 21.55 - 364.86R_{1462} + 369.07R_{2082} \left(R^2 = 0.721,\ n = 94\right) \quad (5)$$

where *F Sand* is the fine sand percentage and R_{1462} and R_{2082} are reflectances at the 1462 and 2082 nm wavelengths, respectively. *Span* had very poor performing models when a single band was utilised. For example, the following model was the best performing single-wavelength model:

$$Span = 2.15 - 2.43R_{2038} \left(R^2 = 0.183,\ n = 94\right) \quad (6)$$

where R_{2038} is the reflectance at the 2038 nm wavelength. A multilinear model can be developed using highly correlated wavelengths ranging between 852 and 2450 nm, as shown below:

$$Span = 1.68 - 24.66R_{852} + 29.62R_{952} + 59.44R_{2252} - 131.36R_{2300} + 79.47R_{2350} - 73.27R_{2400} + 62.52R_{2447} \left(R^2 = 0.516,\ n = 94\right) \quad (7)$$

where R_{852}, R_{952}, R_{2252}, R_{2300}, R_{2350}, R_{2400}, and R_{2447} are reflectances at the 852, 952, 2252, 2300, 2350, 2400 and 2447 nm wavelengths, respectively.

Fine sand and *span* are not well predicted using single wavelength models (see Table 4), whereas $CaCO_3$ shows a much stronger relationship. The models were then validated using 40 independent samples that were not used in the model development (Figure 7). It is notable that a multilinear model leads to a better fit between measured and estimated values.

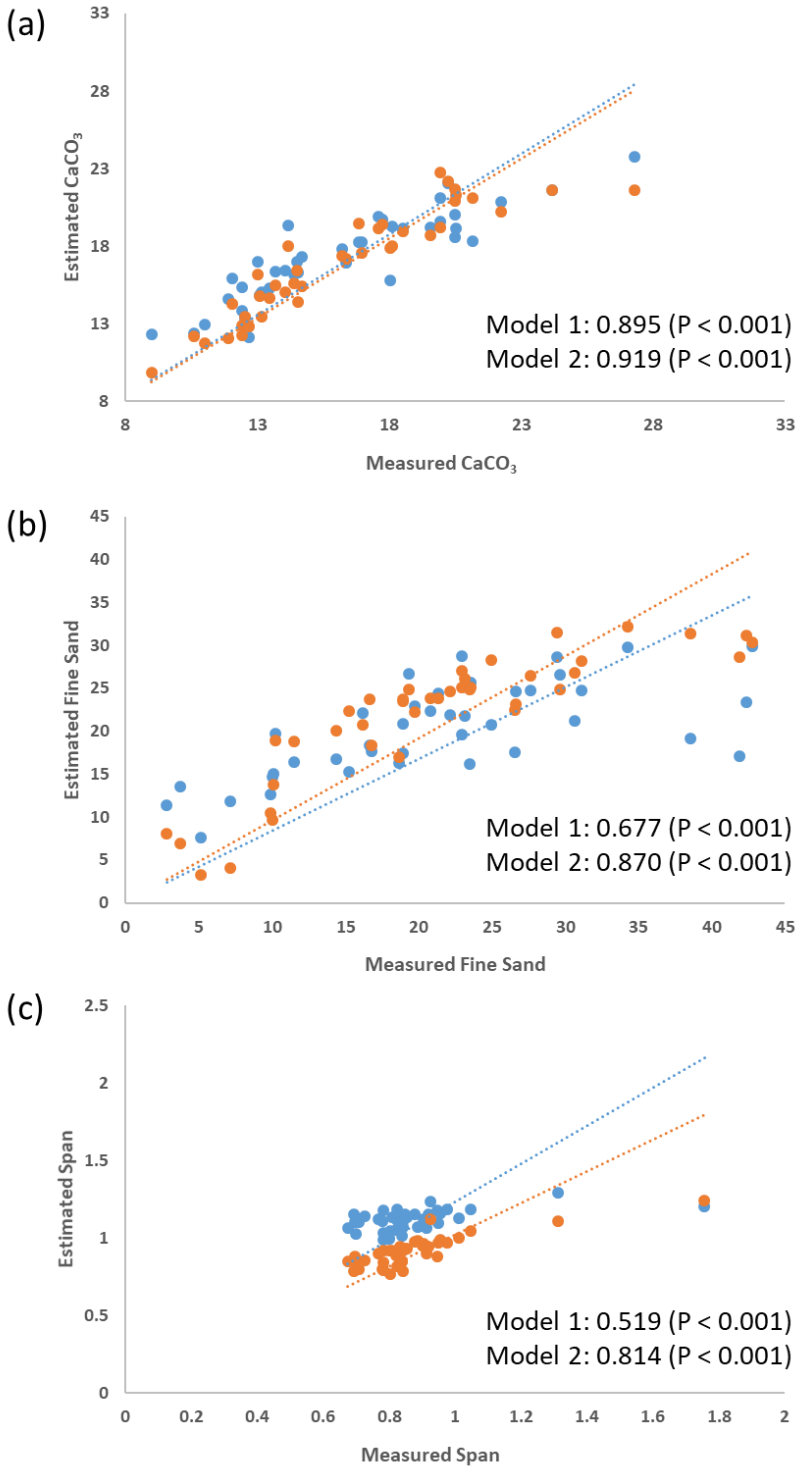

Figure 7. Relationship between estimated and measured (**a**) $CaCO_3$, (**b**) fine sand %, and (**c**) *span* using a linear single wavelength model (model 1) and multilinear model (model 2).

Cross-validation of the output of the linear regression model (Table 4) through comparison between predicted and measured samples is shown in Figure 8. R^2 values, adjusted for the number of variables considered in each model, are higher for $CaCO_3$ with decreasing values for fine sand and *span*. An increased degree of scatter reflects the inability of the model to describe all of the sample points, and this is particularly the case for *span* (see Figure 7). Thus, $CaCO_3$ and fine sand values show the most robust statistical relationships to the spectral measurement data.

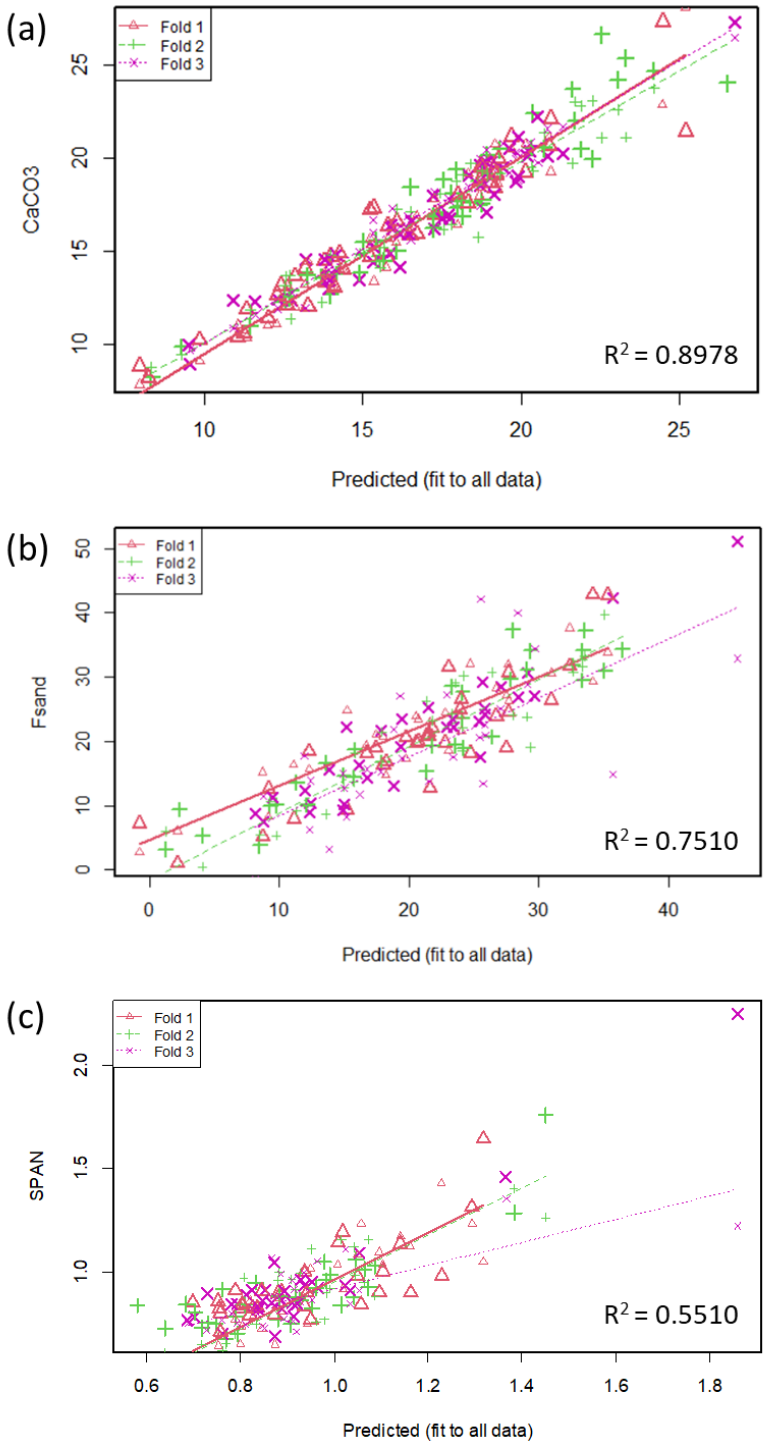

Figure 8. Cross validation results of (**a**) $CaCO_3$ values, (**b**) fine sand and (**c**) *span*. Vertical axes are measured values. Small symbols show cross-validation prediction values.

The spectral characteristics of shell samples 1–5 are presented in Figure 9. Throughout, this shows higher absorption values in the SWIR with consistent dips between all samples at the wavelengths ~1100, 1600 and 2000 nm. The latter may correspond to the water absorption wavelength at ~1950 nm. There is also a very slight jump in reflectance at the water absorption wavelength at ~1450 nm. In addition, the individual shell samples show some variability in the VNIR bands in particular, because of the different shell colours present (Figure 2).

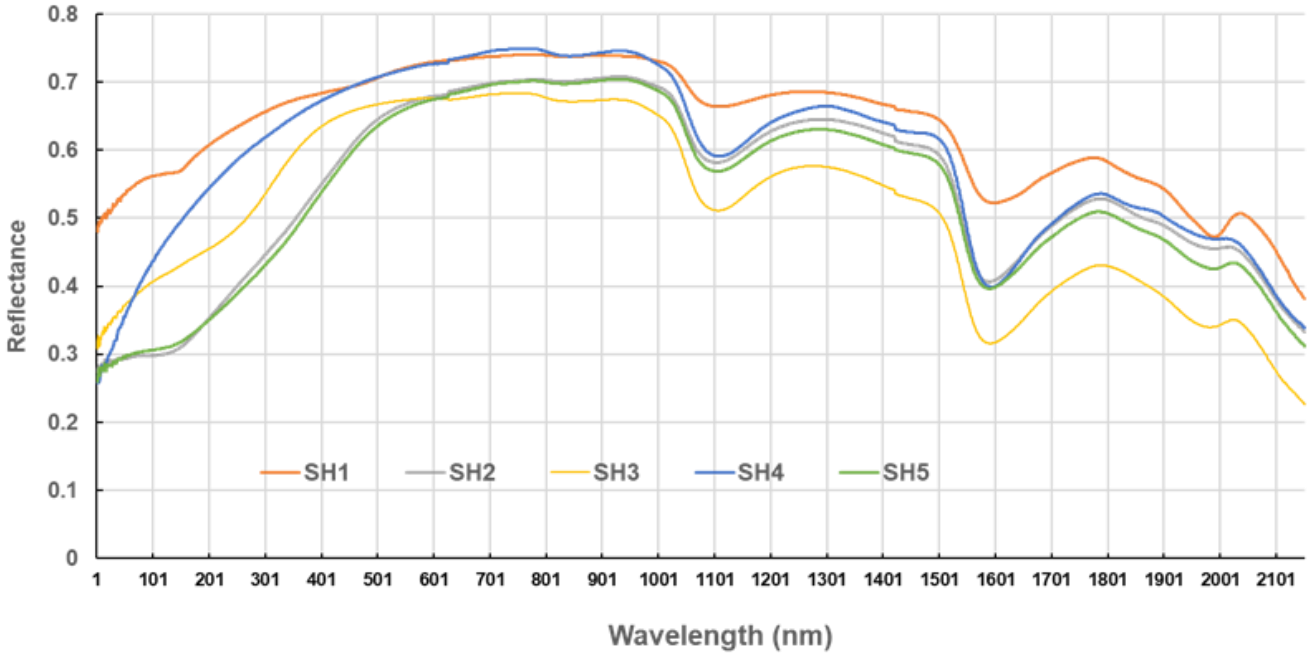

Figure 9. Spectral reflectance results for shell samples (SH) 1–5.

In order to consider whether there are any spectral differences between individual sediment samples with different values of $CaCO_3$, fine sand and *span*, the samples with the highest and lowest values of these parameters (Table 1) are compared to each other (Figure 10). All these samples reflect the aggregated patterns shown in Figure 5a, in which there are decreases in reflectance in the water absorption bands. The samples also show that, irrespective of individual values of $CaCO_3$, fine sand and *span*, there are similar reflectance values in the range 1400–1950 nm (see Figure 6). In more detail, comparison of the $CaCO_3$ values within individual samples shows that shorter wavelengths have a higher reflectance where higher $CaCO_3$ values are present, but that the sample with the lowest $CaCO_3$ values has a higher reflectance at longer wavelengths (Figure 10a). This is mirrored by the results for fine sand (Figure 10b), where the signature for the sample with the lowest amount of fine sand (i.e., the coarsest sample) is very similar to the sample with the highest amount of $CaCO_3$. The reason for this is that broken marine shells (as the source of $CaCO_3$ in the sample) give rise to coarse rather than fine sediment [46]. The parameter *span*, as a reflection of sediment sorting, tends to reflect the presence of coarser outliers in the sample (see the potential autocorrelation with coarse sediment in Table 3) and is therefore of less interpretive significance than either $CaCO_3$ or fine sand (see Figure 8).

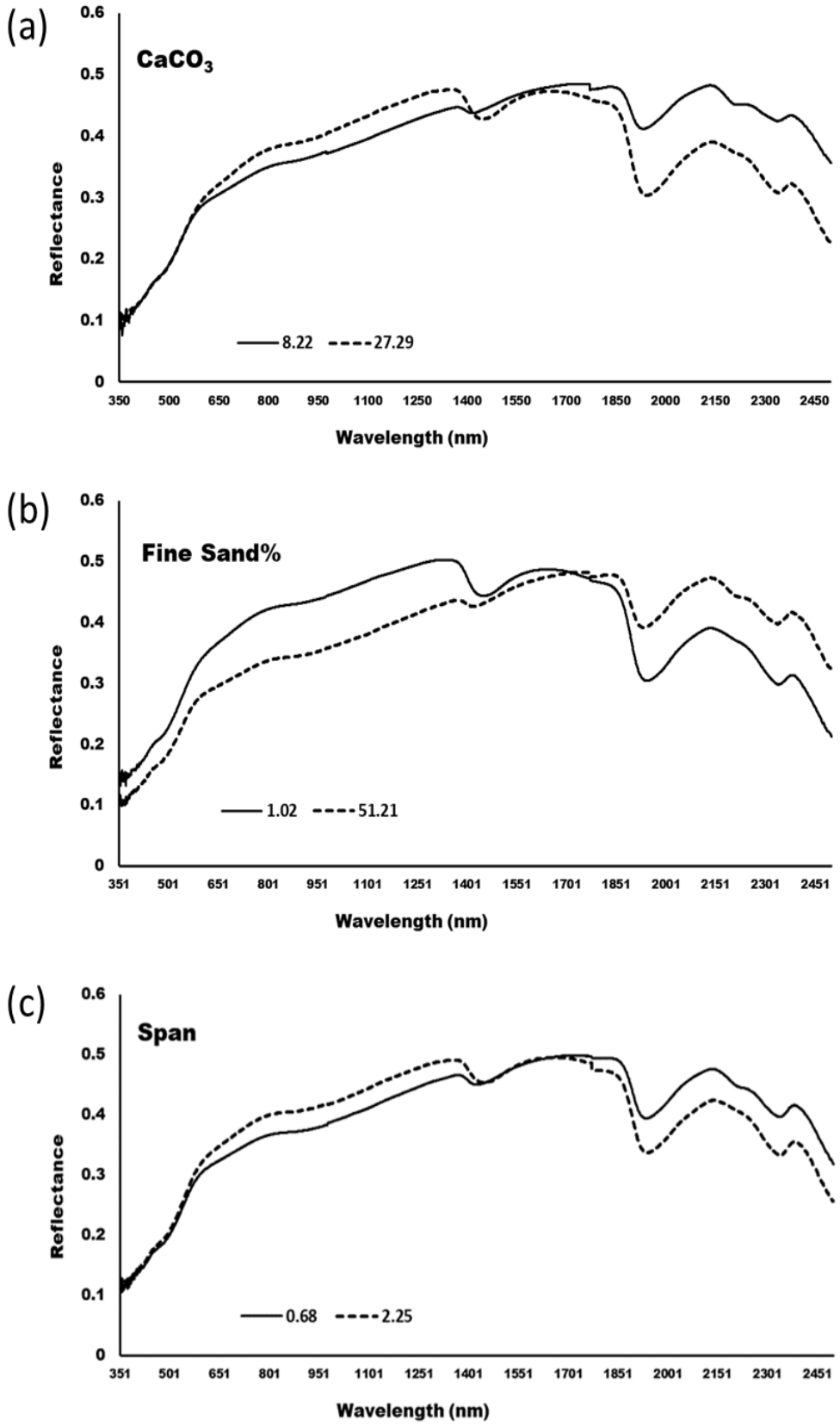

Figure 10. Examples of the spectral signature of individual sediment samples with the greatest range of (**a**) $CaCO_3$ values (highest: #133, lowest: #98); (**b**) *span* values (highest: #61, lowest #139); and (**c**) fine sand percentage (highest #52, lowest #90).

4. Discussion

The presence of a wave-dominated shoreface and wide supratidal zone with migrating transverse dunes (Figures 1 and 4) is typical of the south- and southeast-facing South African coast, in which the dunes have a net eastward migration rate of some 3–12 m yr^{-1} [39,48,49]. Sediment grain size analysis of field samples from Oyster Bay shows that overall they are fairly texturally uniform but with some significant differences in properties between different beach–dune sub-environments (Table 2) and a wide range of carbonate contents (Table 1). The values obtained for grain size properties are similar to other beach–dune systems in the region, e.g., [50,51]. The relatively limited textural and compositional differences mean that it is sometimes difficult to distinguish between such coastal samples, especially in wave-dominated shoreface environments and wind-affected supratidal environments, where sediments are relatively well sorted e.g., [2,4,11,52]. This is certainly the case with beach–dune sediments along the South African coast, e.g., [39,45,49,51,53]. However, detailed statistical analysis shows that different landforms and beach–dune settings at Oyster Bay have different sediment properties (Table 2). This is particularly the case with grain size endmembers (fine and coarse sand) and $CaCO_3$ values that reflect the presence of broken marine shells (not land snail shells) and thus a shoreface source. It is also notable that there are similar overall spectral signatures of all samples (Figure 5), irrespective of their depositional environment (Table 2), which means that the depositional environment of any one sediment sample cannot be resolved by their spectral signature alone. One potential reason for this is that all of the field sediment samples examined here are quartz-dominated (data not shown) and thus, variations in mineralogy cannot be considered as a significant control on their spectral signatures, unlike in previous studies, e.g., [29,47,54]. Although the spectral signature of interstitial water is a dominant feature in other previous studies of coastal sediments e.g., [25,26,32], we deliberately excluded this by drying the samples prior to analysis. This enabled the spectral data of the Oyster Bay samples to be a better representation of grain size and $CaCO_3$ properties (Figure 6), which is the primary aim of this study.

Spectral characteristics of sand systems (beaches, dunes and deserts) have been examined in several studies, e.g., [54,55], and these highlight the potential application of spectral analysis techniques to inform on, in particular, mineralogy and depositional environments [29,32,34–36,47]. Similar to this study, the VNIR part of the spectrum has been previously identified as the most useful in terms of sediment discrimination [55]. There are fewer studies, however, that have looked at grain size data and $CaCO_3$ content. In detail, the spectral reflectance of these samples, however, revealed some fundamental differences between $CaCO_3$ content, fine sand proportion and *span* (Figure 6). These properties also show statistically significant correlations with certain wavelengths (Table 4). However, despite the evidence for some differences in spectral reflectance at different wavelengths for samples with different values of $CaCO_3$ and fine sand (Figure 10), this does not mean that spectral reflectance can be used to predict values of these sediment properties in unknown samples. This is because measured reflectance values at any wavelength are the net result of all grains within the entire sample and not one single component such as shell fragments. In addition, detrital sediment samples of different provenance or found in different depositional environments could have a range of lithologies, water, organic content or other materials, such as microplastics, that may affect spectral reflectance, e.g., [56]. Previous field studies also show the spectral dominance of water absorption signals, e.g., [18,25], and these tend to drown out any signals related to sediment grain size or CaCO3, hence the methodology applied in this study.

These results and their caveats highlight that the potential for spatial mapping of sediment properties across beach–dune environments using hyperspectral imaging techniques may be challenging because of (1) the uncertainties associated with the interpretation of spectral signatures, even under laboratory conditions, and (2) the multiple environmental factors that may be present in a natural beach–dune environment and that may also affect spectral reflectance signatures, including microtopography, vegetation/algae, and salt and

water content. Studies on tidal flats also highlight specific problems related to silt and mud particles and chlorophyll content [25,30,35], and these also have to be considered along coastlines that may contain many different types of depositional settings, as well as the spatial transitions between them.

5. Conclusions

This study, based on field samples from a South African beach–dune system, shows both the complexity and potential of hyperspectral techniques to analyse the properties of these samples (with respect to grain size and $CaCO_3$ content), and their limitations. The major conclusions from this study are:

Statistically, $CaCO_3$, fine sand and *span* are the most important sediment properties in terms of their ability to distinguish between coastal depositional environments (Table 3);

These properties in particular have distinctive spectral signatures in different parts of the VNIR and SWIR wavebands (Table 4);

Fine sand and $CaCO_3$ in particular are clearly distinguishable at ~1850–2450 nm in the SWIR waveband (Figure 6);

Shell content (giving rise to $CaCO_3$ values) and different shell types show somewhat different spectral signatures (Figure 9).

It is notable that previous studies have not described these sediment properties using such analytical techniques and in such a level of detail. The results from this study provide the basis for working towards the automated mapping of a beach–dune environment using hyperspectral satellite data, which must be seen as a long-term goal vital for ongoing monitoring of climate change-sensitive environments.

Author Contributions: Conceptualization, J.K.; Formal analysis, M.A.M.A.E.; Investigation, J.K.; Methodology, J.K.; Software, M.A.M.A.E.; Visualization, M.A.M.A.E.; Writing—original draft, J.K.; Writing—review & editing, M.A.M.A.E. All authors have read and agreed to the published version of the manuscript.

Funding: This research received no external funding.

Institutional Review Board Statement: Not applicable.

Informed Consent Statement: Not applicable.

Data Availability Statement: Data are available from the corresponding author.

Conflicts of Interest: The authors declare no conflict of interest.

References

1. De Lange, W.P.; Healy, T.R.; Darlan, Y. Reproducibility of sieve and settling tube textural determinations for sand-sized beach sediment. *J. Coast. Res.* **1997**, *13*, 73–80.
2. Kasper-Zubillaga, J.J.; Ortiz-Zamora, G.; Dickinson, W.W.; Urrutia-Fucugauchi, J.; Soler-Arechalde, A.M. Textural and compositional controls on modern beach and dune sands, New Zealand. *Earth Surf. Proc. Landf.* **2007**, *32*, 366–389. [CrossRef]
3. Kwarteng, A.Y.; Al-Hatrushi, S.M.; Illenberger, W.K.; McLachlan, A. Grain size and mineralogy of Al Batinah beach sediments, Sultanate of Oman. *Arab. J. Geosci.* **2016**, *9*, 557. [CrossRef]
4. Hallin, C.; Almström, B.; Larson, M.; Hanson, H. Longshore transport variability of beach face grain size: Implications for dune evolution. *J. Coastal Res.* **2019**, *35*, 751–764. [CrossRef]
5. Pyökäri, M. Beach Sediments of Crete: Texture, Composition, Roundness, Source and Transport. *J. Coast. Res.* **1999**, *15*, 537–553.
6. Smith, D.A.; Cheung, K.F. Empirical relationships for grain size parameters of calcareous sand on Oahu, Hawaii. *J. Coast. Res.* **2002**, *18*, 82–93.
7. Alsharhan, A.S.; El-Sammak, A.A. Grain size analysis and characterization of sedimentary environments of the United Arab Emirates coastal area. *J. Coast. Res.* **2004**, *20*, 464–477. [CrossRef]
8. Deidun, A.; Gauci, R.; Schembri, J.A.; Šegina, E.; Gauci, A.; Gianni, J.; Gutierrez, J.A.; Sciberras, A.; Sciberras, J. Comparative median grain size assessment through three different techniques for sandy beach deposits on the Maltese Islands (Central Mediterranean). *J. Coast. Res.* **2013**, *65*, 1757–1761. [CrossRef]
9. Poizot, E.; Anfuso, G.; Méar, Y.; Bellido, C. Confirmation of beach accretion by grain-size trend analysis: Camposoto beach, Cádiz, SW Spain. *Geo-Mar. Lett.* **2013**, *33*, 263–272. [CrossRef]

10. Choi, T.J.; Choi, J.Y.; Park, J.Y.; Um, H.Y.; Choi, J.H. The Effects of Nourishments Using the Grain-Size Trend Analysis on the Intertidal Zone at a Sandy Macrotidal Beach. *J. Coast. Res.* **2018**, *85*, 426–430. [CrossRef]
11. Gunaratna, T.; Suzuki, T.; Yanagishima, S. Cross-shore grain size and sorting patterns for the bed profile variation at a dissipative beach: Hasaki Coast, Japan. *Mar. Geol.* **2019**, *407*, 111–120. [CrossRef]
12. Pedreros, R.; Howa, H.L.; Michel, D. Application of grain size trend analysis for the determination of sediment transport pathways in intertidal areas. *Mar. Geol.* **1996**, *135*, 35–49. [CrossRef]
13. Edwards, A.C. Grain Size and Sorting in Modern Beach Sands. *J. Coast. Res.* **2001**, *17*, 38–52.
14. Gallagher, E.L.; MacMahan, J.; Reniers, A.J.H.M.; Brown, J.; Thornton, E.B. Grain size variability on a rip-channeled beach. *Mar. Geol.* **2011**, *287*, 43–53. [CrossRef]
15. Pradhan, U.K.; Sahoo, R.K.; Pradhan, S.; Mohany, P.K.; Mishra, P. Textural Analysis of Coastal Sediments along East Coast of India. *J. Geol. Soc. India* **2020**, *95*, 67–74. [CrossRef]
16. Deronde, B.; Kempeneers, P.; Forster, R.M. Imaging spectroscopy as a tool to study sediment characteristics on a tidal sandbank in the Westerschelde. *Estuar. Coast. Shelf Sci.* **2006**, *69*, 580–590. [CrossRef]
17. Castillo, E.; Pereda, R.; de Luis, J.M.; Medina, R.; Viguri, J. Sediment grain size estimation using airborne remote sensing, field sampling, and robust statistic. *Environ. Monit. Assess.* **2011**, *181*, 431–444. [CrossRef]
18. Manzo, C.; Valentini, E.; Taramelli, A.; Filipponi, F.; Disperati, L. Spectral characterization of coastal sediments using Field Spectral Libraries, Airborne Hyperspectral Images and Topographic LiDAR Data (FHyL). *Int. J. Appl. Earth Obs. Geoinf.* **2015**, *36*, 54–68. [CrossRef]
19. Ibrahim, E.; Kim, W.; Crawford, M.; Monbaliu, J. A regression approach to the mapping of bio-physical characteristics of surface sediment using in situ and airborne hyperspectral acquisitions. *Ocean. Dyn.* **2017**, *67*, 299–316. [CrossRef]
20. Smit, Y.; Ruessink, G.; Brakenhoff, L.B.; Donker, J.J.A. Measuring spatial and temporal variation in surface moisture on a coastal beach with a near-infrared terrestrial laser scanner. *Aeolian Res.* **2018**, *31*, 19–27. [CrossRef]
21. Kim, K.-L.; Kim, B.-J.; Lee, Y.-K.; Ryu, J.-H. Generation of a Large-Scale Surface Sediment Classification Map Using Unmanned Aerial Vehicle (UAV) Data: A Case Study at the Hwang-do Tidal Flat, Korea. *Remote Sens.* **2019**, *11*, 29. [CrossRef]
22. Jacq, K.; Giguet-Covex, C.; Sabatier, P.; Perrette, Y.; Fanget, B.; Coquin, D.; Debret, M.; Arnaud, F. High-resolution grain size distribution of sediment core with hyperspectral imaging. *Sediment. Geol.* **2019**, *393–394*, 105536. [CrossRef]
23. Ghanbari, H.; Jacques, O.; Adaïmé, M.É.; Gregory-Eaves, I.; Antoniades, D. Remote Sensing of Lake Sediment Core Particle Size Using Hyperspectral Image Analysis. *Remote Sens.* **2020**, *12*, 3850. [CrossRef]
24. Zander, P.D.; Wienhues, G.; Grosjean, M. Scanning Hyperspectral Imaging for In Situ Biogeochemical Analysis of Lake Sediment Cores: Review of Recent Developments. *J. Imaging* **2022**, *8*, 58. [CrossRef]
25. Ryu, J.-H.; Na, Y.-H.; Won, J.-S.; Doerffer, R. A critical grain size for Landsat ETM+ investigations into intertidal sediments: A case study of the Gomso tidal flats, Korea. *Estuar. Coast. Shelf Sci.* **2004**, *60*, 491–502. [CrossRef]
26. Small, C.; Steckler, M.; Seeber, L.; Akhter, S.H.; Goodbred, S., Jr.; Mia, B.; Imam, B. Spectroscopy of sediments in the Ganges–Brahmaputra delta: Spectral effects of moisture, grain size and lithology. *Remote Sens. Environ.* **2009**, *113*, 342–361. [CrossRef]
27. Legleiter, C.J.; Stegman, T.K.; Overstreet, B.T. Spectrally based mapping of riverbed composition. *Geomorphology* **2016**, *264*, 61–79. [CrossRef]
28. Ciampalini, A.; Consoloni, I.; Salvatici, T.; Di Traglia, F.; Fidolini, F.; Sarti, G.; Moretti, S. Characterization of coastal environment by means of hyper- and multispectral techniques. *Appl. Geogr.* **2015**, *57*, 120–132. [CrossRef]
29. Rejith, R.G.; Sundararajan, M.; Gnanappazham, L.; Loveson, V.J. Satellite-based spectral mapping (ASTER and Landsat data) of mineralogical signatures of beach sediments: A precursor insight. *Geocarto Int.* **2022**, 1–24, *in press*. [CrossRef]
30. Park, N.-W.; Jang, D.-H.; Chi, K.-H. Integration of IKONOS imagery for geostatistical mapping of sediment grain size at Baramarae beach, Korea. *Int. J. Remote Sens.* **2009**, *30*, 5703–5724. [CrossRef]
31. Williams, K.K.; Greeley, R. Laboratory and field measurements of the modification of radar backscatter by sand. *Remote Sens. Environ.* **2004**, *89*, 29–40. [CrossRef]
32. Van der Wal, D.; Herman, P.M.J. Regression-based synergy of optical, shortwave infrared and microwave remote sensing for monitoring the grain-size of intertidal sediments. *Remote Sens. Environ.* **2007**, *111*, 89–106. [CrossRef]
33. Rainey, M.P.; Tyler, A.N.; Gilvear, D.J.; Bryant, R.G.; McDonald, P. Mapping intertidal estuarine sediment grain size distributions through airborne remote sensing. *Remote Sens. Environ.* **2003**, *86*, 480–490. [CrossRef]
34. Choi, J.K.; Ryu, J.H.; Eom, J. Integration of spatial variables derived from remotely sensed data for the mapping of the tidal surface sediment distribution. *J. Coast. Res.* **2011**, *64*, 1653–1657.
35. Ibrahim, E.; Monbaliu, J. Suitability of spaceborne multispectral data for inter-tidal sediment characterization: A case study. *Estuar. Coast. Shelf Sci.* **2011**, *92*, 437–445. [CrossRef]
36. Park, N.-W. Geostatistical integration of field measurements and multi-sensor remote sensing images for spatial prediction of grain size of intertidal surface sediments. *J. Coast. Res.* **2019**, *SI90*, 190–196. [CrossRef]
37. Wepener, V.; Degger, N. South Africa. In *World Seas: An Environmental Evaluation: Volume II: The Indian Ocean to the Pacific*, 2nd ed.; Sheppard, C., Ed.; Elsevier: Amsterdam, The Netherlands, 2019; pp. 101–119.
38. Meeuwis, J.; van Rensburg, P.A.J. Logarithmic spiral coastlines: The northern Zululand coastline. *S. Afr. Geogr. J.* **1986**, *68*, 18–44. [CrossRef]

39. Knight, J.; Burningham, H. The morphodynamics of transverse dunes on the coast of South Africa. *Geo-Mar. Lett.* **2021**, *41*, 47. [CrossRef]
40. Roberts, D.L.; Botha, G.A.; Maud, R.R.; Pether, J. Coastal Cenozoic Deposits. In *The Geology of South Africa*; Johnson, M.R., Anhaeusser, C.R., Thomas, R.J., Eds.; Geological Society of South Africa/Council for Geoscience: Johannesburg/Pretoria, South Africa, 2006; pp. 605–628.
41. Claassen, D. Geographical controls on sediment accretion of the Cenozoic Algoa Group between Oyster Bay and St. Francis, Eastern Cape coastline, South Africa. *S. Afr. J. Geol.* **2014**, *117*, 109–128. [CrossRef]
42. Knight, J. The late Quaternary stratigraphy of coastal dunes and associated deposits in South Africa. *S. Afr. J. Geol.* **2021**, *124*, 995–1006. [CrossRef]
43. Butzer, K.W.; Helgren, D.M. Late Cenozoic evolution of the Cape coast between Knysna and Cape St. Francis, South Africa. *Quat. Res.* **1972**, *2*, 143–169. [CrossRef]
44. Rossel, R.A.V.; McBratney, A.B. Laboratory evaluation of a proximal sensing technique for simultaneous measurement of soil clay and water content. *Geoderma* **1998**, *85*, 19–39. [CrossRef]
45. Schumann, E.H.; Illenberger, W.K.; Goschen, W.S. Surface winds over Algoa Bay, South Africa. *S. Afr. J. Sci.* **1991**, *87*, 202–207.
46. Carter, R.W.G. Some problems associated with the analysis and interpretation of mixed carbonate and quartz beach sands, illustrated by examples from north-west Ireland. *Sediment. Geol.* **1982**, *33*, 35–56. [CrossRef]
47. Fang, Q.; Hong, H.; Zhao, L.; Kukolich, S.; Yin, K.; Wang, C. Visible and Near-Infrared Reflectance Spectroscopy for Investigating Soil Mineralogy: A Review. *J. Spectroscop.* **2018**, *2018*, 3168974. [CrossRef]
48. Lubke, R.A.; Sugden, J. Short-term change in mobile dunes at Port Alfred, South Africa. *Environ. Manag.* **1990**, *14*, 209–220. [CrossRef]
49. Knight, J.; Burningham, H. Sand dunes and ventifacts on the coast of South Africa. *Aeolian Res.* **2019**, *37*, 44–58. [CrossRef]
50. Harmse, J.T. Trend surface analysis of aeolian sand movement on the southwest African coast. *S. Afr. Geogr. J.* **1985**, *67*, 31–39. [CrossRef]
51. Illenberger, W.K. Variations of sediment dynamics in Algoa Bay during the Holocene. *S. Afr. J. Sci.* **1993**, *89*, 187–196.
52. Çelikoğlu, Y.; Yüksel, Y.; Kabdaşlı, M.S. Cross-shore sorting on a beach under wave action. *J. Coast. Res.* **2006**, *22*, 487–501. [CrossRef]
53. Olivier, M.J.; Garland, G.G. Short-term monitoring of foredune formation on the east coast of South Africa. *Earth Surf. Proc. Landf.* **2003**, *28*, 1143–1155. [CrossRef]
54. Bandfield, J.L.; Edgett, K.S.; Christensen, P.R. Spectroscopic study of the Moses Lake dune field, Washington: Determination of compositional distributions and source lithologies. *J. Geophys. Res.* **2002**, *107*, 5092. [CrossRef]
55. Sadiq, A.; Howari, F. Remote Sensing and Spectral Characteristics of Desert Sand from Qatar Peninsula, Arabian/Persian Gulf. *Remote Sens.* **2009**, *1*, 915–933. [CrossRef]
56. Moshtaghi, M.; Knaeps, E.; Sterckx, S.; Garaba, S.; Meire, D. Spectral reflectance of marine macroplastics in the VNIR and SWIR measured in a controlled environment. *Sci. Rep.* **2021**, *11*, 5436. [CrossRef] [PubMed]